Robust antibacterial activity of xanthan-gum-stabilized and patterned CeO_{2-x}-TiO_2 anti-fog films

Fangwei Guo[1, 2, 3]*, Fei Pan[4,#], Wenchen Zhang[1], Tian Liu[2], Flavia Zuber[3], Xing Zhang[5], Yali Yu[1], Ruiji Zhang[1], Markus Niederberger[3], Qun Ren[4]

[1]Shanghai Key Laboratory of Advanced High-temperature Materials and Precision Forming, School of Materials Science and Engineering, Shanghai Jiao Tong University, 200240 Shanghai, China

[2]Shanghai Key Laboratory of Spacecraft Mechanism, 201108 Shanghai, China

[3]Laboratory for Multifunctional Materials, Department of Materials, ETH Zürich, Vladimir-Prelog-Weg 5, 8093 Zürich, Switzerland

[4]Laboratory for Biointerfaces, Empa, Swiss Federal Laboratories for Materials Science and Technology, Lerchenfeldstrasse 5, 9014 St. Gallen, Switzerland

[5]Shanghai Institute of Aerospace System Engineering, 201108 Shanghai, China

*E-mail: fwguo2014@sjtu.edu.cn (FG)

[#]Present address: Department of Chemistry, University of Basel, Mattenstrasse 24a, BPR 1096, 4058 Basel, Switzerland.

Abstract

Increased occurrence of antimicrobial resistance leads to a huge burden on patients, the healthcare system, and society worldwide. Developing antimicrobial materials through doping rare-earth elements is a new strategy to overcome this challenge. To this end, we design antibacterial films containing CeO_{2-x}-TiO_2, xanthan-gum, poly (acrylic acid), and hyaluronic acid. The CeO_{2-x}-TiO_2 inks are additionally integrated into a hexagonal grid for prominent transparency. Such design yields not only an antibacterial efficacy of approximately 100 % toward *Staphylococcus aureus* and *Escherichia coli* but also excellent anti-fog performance for 72 h in a 100 % humidity atmosphere. Moreover, FluidFM is employed to understand the interaction in-depth between bacteria and materials. We further reveal that reactive oxygen species (ROS) are crucial for the bactericidal activity of *E. coli* through fluorescent spectroscopic analysis and SEM imaging. We meanwhile confirm that Ce^{3+} ions are involved in the stripping phosphate groups, damaging the cell membrane of *S. aureus*. Therefore, the hexagonal mesh and xanthan-gum cross-linking chains act as a reservoir for ROS and Ce^{3+} ions, realizing a long-lasting antibacterial function. We hence develop an antibacterial and anti-fog dual-functional material that has the potential for a broad application in display devices, medical devices, food packaging, and wearable electronics.

Keywords: CeO_{2-x}-TiO_2 grid film, antibacterial activity, anti-fog, coating bonding strength, photo-activation,

1. Introduction

Bacterial colonization on surfaces and the subsequent biofilm formation, especially in medical devices, food packaging, wearable electronics, or textile industries, can lead to severe infections and mortality[1-4]. Moreover, the formation of a fogging film on a substrate can not only blur vision causing inconvenience in daily usage but also lead to fatal risks during surgery[3, 5, 6]. Therefore, antibacterial and anti-fog properties are preferable for healthcare when designing functional polymer materials[7-10]. However, hydrophobic surfaces used as anti-fog contain a number of non-polar groups and textures, which could accelerate bacteria adhesion and proliferation[8, 10]. Additionally, the emergence of antimicrobial-resistant bacteria due to overuse and abuse of antibiotics brings difficulties in defeating bacterial infections. Therefore, an effective antibacterial surface of a dedicated design is necessary to efficiently fight bacterial infections [1, 11].

Among various antibacterial materials, Ag nanoparticles embedded in films have prominent antimicrobial properties, but the oxidation of silver is detrimental to the antibacterial activity[2, 3, 12, 13]. However, modified surfaces, which can release antimicrobial agents or metal ions (Ag^+, Cu^{2+}, and Zn^{2+}) to inhibit bacterial colonization, can cause critical issues such as cytotoxicity, short antimicrobial durability, and resistance[12-14]. Contact-killing surfaces exploit either incorporated natural macromolecules, *e.g.*, polysaccharides[15], or material surfaces (*e.g.*, TiO_2) [16], generating reactive oxygen species (ROS) to confer antibacterial activity[14, 15]. The ROS concentration and the resultant antibacterial efficacy on TiO_2-based surfaces rely on the duration of UV irradiation and humid surrounding[16-18]. However, both Ag^+ ions and ROS manifest better antibacterial activity toward *E. coli* than *S. aureus*, likely caused by different bacterial membrane structures[2, 12, 13, 16].

CeO_2 is drawing more and more attention in the biomedical industry thanks to its antioxidant, antibacterial, anticancer, and biocompatibility properties[19, 20]. In addition, the TiO_2 nanoparticles doped with CeO_2 display an improved photocatalysis and photo-induced hydrophilicity in the visible spectrum compared with the anatase TiO_2 with a band-gap of 3.2-3.35 eV, which is attributed to the lower band-gap (2.9-3.2eV) of CeO_2[21, 22]. Noteworthily, the Ce^{3+}/Ce^{4+} redox couple can easily switch between two states ($CeO_2 \leftrightarrow CeO_{2-x} + x/2O_2$), which is crucial for ceria nanoparticles manifesting catalytic activity, enzyme-like activities, and germ-killing[19, 23, 24]. CeO_2 nanoparticles with high Ce^{3+} content usually have abundant oxygen vacancies, facilitating oxygen exchange and redox reactions. However, the antimicrobial activity and durability of Gram-positive bacteria remain to be revealed due to an ambiguous understanding of the antibacterial mechanism[19, 20, 24, 25]. In this work, the CeO_{2-x}-TiO_2 films

stabilized by the xanthan-gum were prepared using a micro-stamping method with three different patterns. Effects of the Ce/Ti molar ratios and mesh patterns on antibacterial activity, optical properties, bacteria adhesion, interface adhesion, surface hydrophilicity, and fogging resistance were systematically investigated, and the long-lasting antibacterial mechanism was explored.

2. Results and discussion

2.1. Morphology and composition of as-synthesized CeO_{2-x}-TiO_2 particles

The morphologies and lattice structures of the as-synthesized CeO_{2-x}, TiO_2, and 75 mol% CeO_{2-x}-TiO_2 particles (containing 75 mol% CeO_{2-x}) were analyzed and displayed with representative images in Figure 1a-f. Additions of the CeO_{2-x} reduced the crystalline size of pure CeO_{2-x} and TiO_2 (Figure 1a&d). The crystalline size of the 75 mol% CeO_{2-x}-TiO_2 particles was 3-5nm (Figure 1f). The 25 mol% CeO_{2-x}-TiO_2 and 50 mol% CeO_{2-x}-TiO_2 systems led to transmission electron microscopy (TEM) images and X-ray diffraction (XRD) similar to the 75 mol% CeO_{2-x}-TiO_2. The loose CeO_{2-x}-TiO_2 nanoparticles benefit the Ce^{3+} preservation and the related photocatalytic effect[26], which are the advantages of using the microwave reaction method in the Benzyl alcohol bath. With an increasing ratio of CeO_{2-x}, TiO_2 crystallinity became lower (Figure 1g), displaying an amorphous-like structure (Figure 1f).

XRD patterns revealed that the TiO_2 system yielded a single anatase phase (Figure 1g). However, the further addition of the Ce precursor decreased the anatase TiO_2. In the presence of CeO_{2-x}, the absorption spectrum of TiO_2 shifted from the UV to the Vis light range (wavelength >372 nm) according to the UV-Vis absorption spectrum in Figure 1h. The UV-Vis absorption spectrum of the 75 mol% CeO_{2-x}-TiO_2 particles showed high absorbance at 400-800 nm. The absorption edges shifted to the Vis region, and the high absorbance for 75 mol% CeO_{2-x}-TiO_2 particles indicated that these particles have narrower band gaps than the TiO_2 particles. Thus, the 75 mol% CeO_{2-x}-TiO_2 particles exhibited stronger photocatalytic activity under visible light. The high-resolution X-ray photoelectron spectroscopy (XPS) spectra of Ti 2p and Ce 3d acquired from the TiO_2 and CeO_{2-x}-TiO_2 particles are displayed in Figure 1i&j. The measured binding energies of the Ti $2p^{3/2}$ peaks of the TiO_2, CeO_{2-x}, and 75 mol% CeO_{2-x}-TiO_2 particles after surface charging corrections were 457.8 ± 0.02 eV and 457.5 ± 0.02 eV, respectively. The corresponding binding energies of the Ti $2p^{1/2}$ peaks were measured at 463.5 ± 0.02 eV and 463.2 ± 0.02 eV, respectively. The binding energies and the separation between the two peaks at 5.70 ± 0.02 eV were close to the reported values[27, 28]. According to

the deconvolution results, the Ti 2p spectrum of the 75 mol% CeO_{2-x}-TiO_2 particles was mainly caused by the Ti^{4+} oxidation state and slightly contributed by the reduced species Ti^{3+}, which is assigned to Ti^{3+} $2p^{3/2}$ and appears at a lower binding energy of 456.6 ± 0.02 eV (black arrow). The peaks located at 904.6 eV, 885.6 eV, and 880.8 eV corresponded to Ce^{3+} and the peaks at 917.0 eV, 907.5 eV, 901.1 eV, 898.4 eV, 889.3 eV, and 882.5 eV belonged to Ce^{4+} [19-21, 28]. By integrating high-resolution XPS spectra of Ce 3d, the contents of Ce^{3+} were 44.1 % and 36.8 %, respectively, for the CeO_{2-x} and 75 mol% CeO_{2-x}-TiO_2 particles (Figure S-1). The previous studies[19, 28] have confirmed that nanoceria showed oxidase-like activity, which was attributed to the valence states of Ce^{3+} and Ce^{4+}, as well as oxygen vacancies.

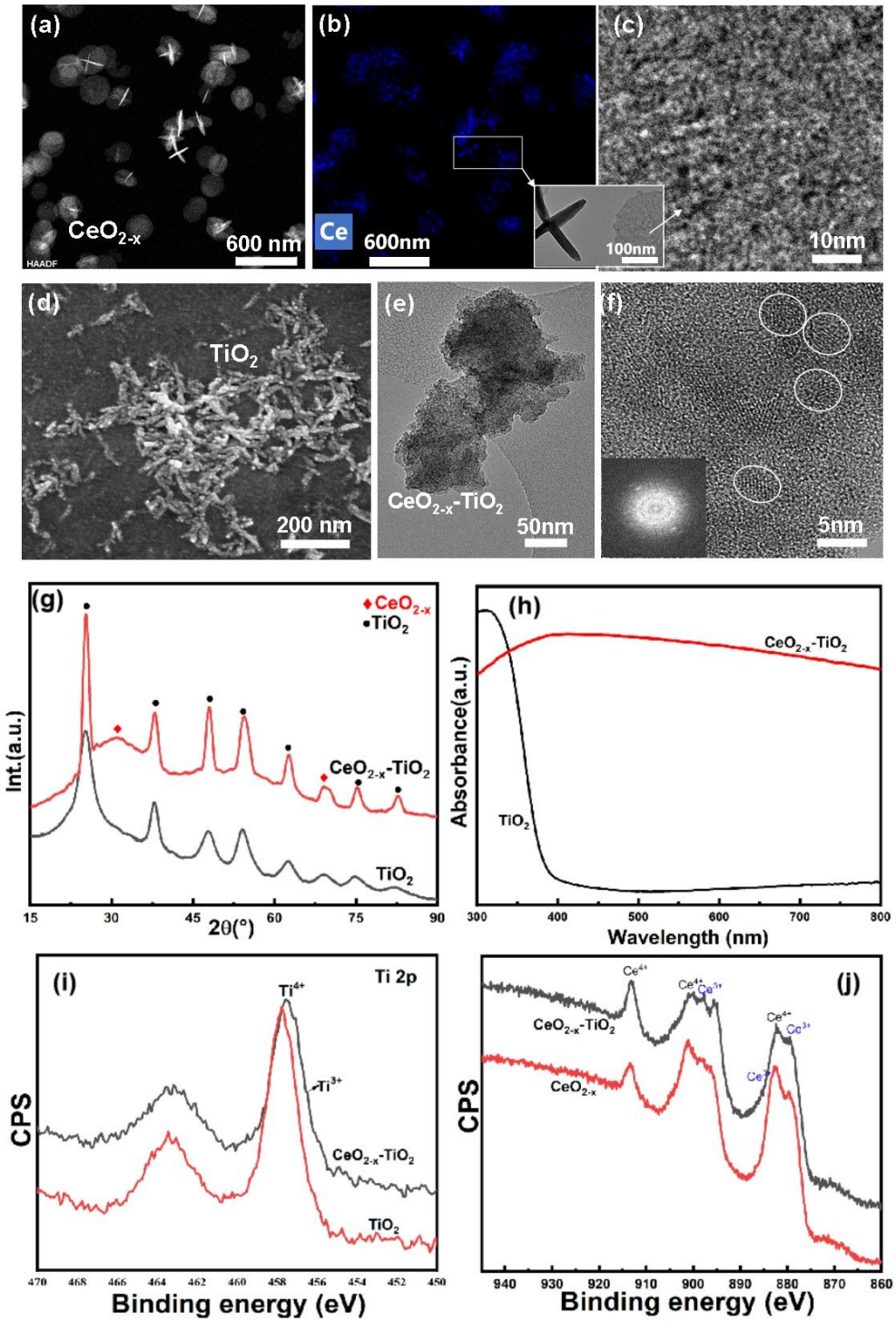

Figure 1. Analysis of the morphology and composition. TEM observation of CeO_{2-x} (a), its corresponding energy dispersive X-ray analysis (EDX) mapping of cerium (b), and the corresponding high-resolution image (c). (d) Morphological analysis of TiO_2 particles by scanning electron microscopy (SEM). (e) 75 mol% CeO_{2-x}-TiO_2 particles and (f) the corresponding high-resolution TEM image with electron diffraction as the inset. (g) X-ray diffraction patterns, (h) UV-Vis absorbance, (i) Ti 2p peaks of XPS and (j) Ce 3d peaks of XPS acquired from TiO_2, CeO_{2-x} and 75 mol % CeO_{2-x}-TiO_2 particles.

2.2. Topographies and transmittance of polymer-CeO_{2-x}-TiO_2 grid films

Three different polydimethylsiloxanes (PDMS) micro-stamps (see Figure 2a-c) were used to prepare grid films on polyethylene terephthalate foils (PET). As illustrated in Figure 2d&e, the grid film was composed of two layers: a framework and a polymer top layer. Figure S-2 shows that the polyvinyl pyrrolidone (PVP) solutions of different concentrations of TiO_2, CeO_{2-x}, and Ag^+ ions (termed S1-S7 inks as described in Table 2 in the experimental methods) were utilized to prepare the framework. The polymer top layer was prepared by using the mixed solution of xanthan-gum (XG), hyaluronic acid (HA), and poly (acrylic acid) (PAA). The average transmission spectra and diffuse transmittance spectra were displayed in Figure 2 f&g, regarding the blank PET foils, the PET foil covered with a single framework, and the grid film prepared with the S7 ink (containing the 75 mol% CeO_{2-x}-TiO_2 particles). The S7 grid film manifested an average transmittance of 84 % and diffuse transmittance of 91.5 % over the visible light range of 380-800 nm, slightly lower than that of the blank PET foil of 95 % average transmittance. Although the color of the S7 grid film was light yellow, the pictures under the grid film remained clear and highly transparent.

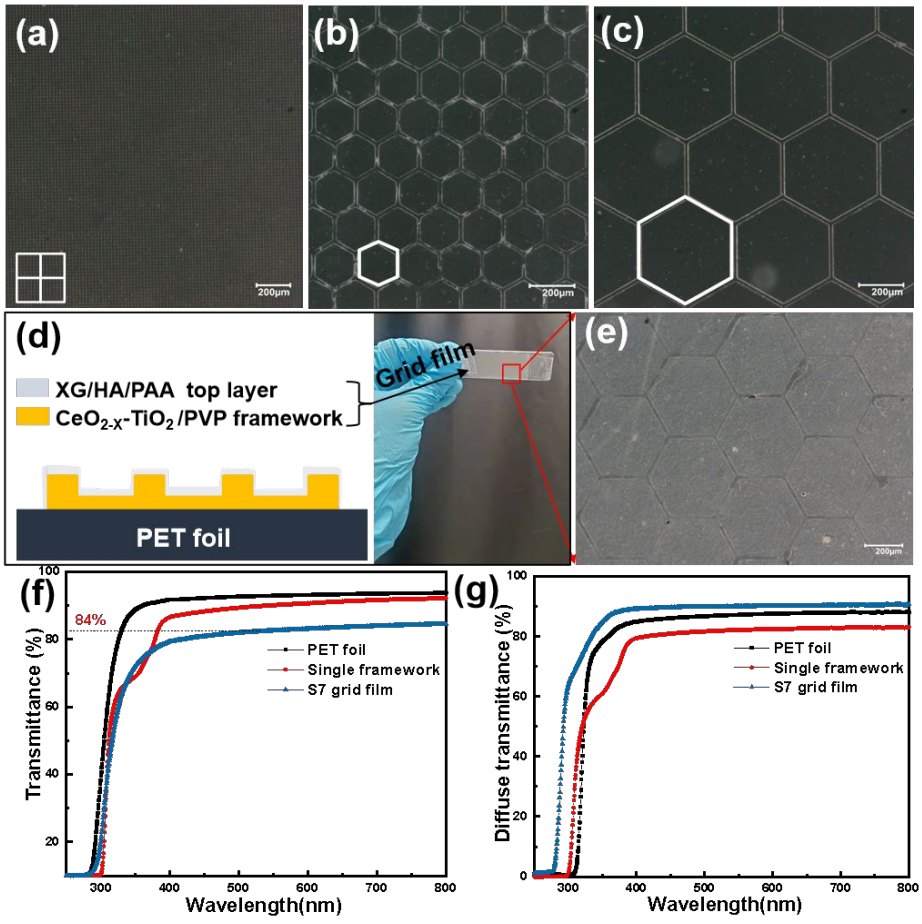

Figure 2. Optical morphology and transparent properties of the grid films. (a-c) Three micro-stamps to prepare the grid films;(d) a schematic and a photo of the grid film. Optical images of (e) the XG/HA/PAA top layer. (f) Transmittance and (g) Diffuse transmittance of a blank PET foil, the PET foil coated with a single framework, and the PET foil coated with the S7 grid film.

The grid films prepared by the two hexagonal mesh stamps exhibited high integrity compared with that prepared by the square mesh stamp (Figure 2a). The surface roughness (Ra=5.2μm) of the grid films prepared by the large hexagonal mesh stamp (Figure 3a, side length a=200 μm, width w=20 μm, and height h=5 μm) was much lower than that of the grid films (Ra=76.5μm) prepared by the small hexagonal mesh stamp (Figure 3e). There were no cracks in both stamp frameworks and on the surface of the large hexagonal grid film. However, penetrated cracks were observed in the small hexagonal grid film due to the drying stress in Figure 3d&h. Therefore, the large hexagonal mesh stamp was used for preparing the grid films in this study.

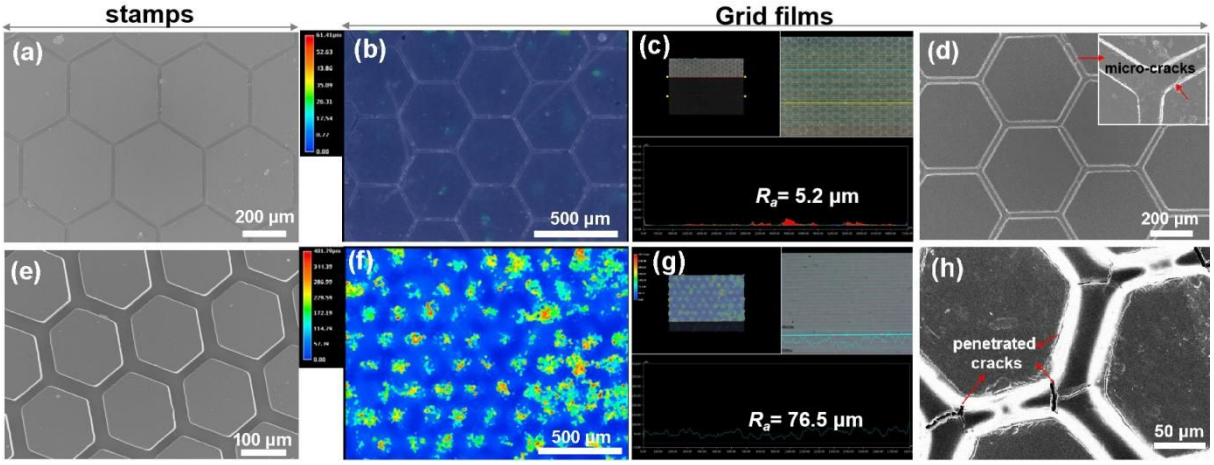

Figure 3. (a) and (e) SEM images of the hexagonal micro-stamps of two different sizes. (b-c) and (f-g) optical images and surface roughness measurements of the two grid films prepared by the two micro-stamps. SEM images of the two grid films with the large hexagonal mesh (d) and the small hexagonal mesh (h), respectively. Figures 3b, c, f, and g were obtained through a non-contact 3D-laser profilometry (ZegageTM, Zygo, USA). The profilometry was utilized to measure the surface roughness of the grid films investigated.

2.3. Bonding strength, surface wettability, and anti-fog of the S7 grid films

The bonding strength of PET foils coated with the S7 grid film was investigated by the tensile testing method (Figure 4a-c). Compared with the blank PET samples, the tensile strength of the PET coated with the S7 grid film increased from 37.3 ± 0.2 MPa to 41.7 ± 0.2 MPa, calculated from the force-displacement curves based on standard ISO 527-1:2012[29, 30]. The enhanced tensile strength was probably due to the rigid chain properties of the 75 mol% CeO_{2-x}-TiO_2/PVP framework, which improved the mechanical property of the PET matrix[30]. The elongation of the coated PET was 76 % larger than that of the blank PET, which was probably caused by the high elasticity of polysaccharide molecular chains of xanthan-gum (XG) (Figure 4d)[31]. The sample modules of bone shape (Figure 4b) and strip-type (Figure 4c) were used to study the bonding strength of the S7 grid film. In the typical force-displacement curves of the

corresponding samples, the loads at the first yield point (see the black arrows) were attributed to the partially detached S7 film from the substrates (Figure 4e&f). Therefore, the loads that reached the first yield point were used to estimate the samples' bonding strength. The bonding strengths of the bone shape samples and the strip-type samples were 5.6 ± 0.12 MPa and 6.1 ± 0.15 MPa, respectively, which indicated that the interface adhesion of the S7 grid film was more robust than most of the antibacterial coatings reported[3, 8, 9, 32]. We noticed that the bone shape sample broke at the neck area (see Figure 4b) when reaching the maximum load rather than breaking at the S7 grid film area in the strip-type sample. This final broken site probably led to the slightly lower bonding strength of bone shape samples than the strip-type samples.

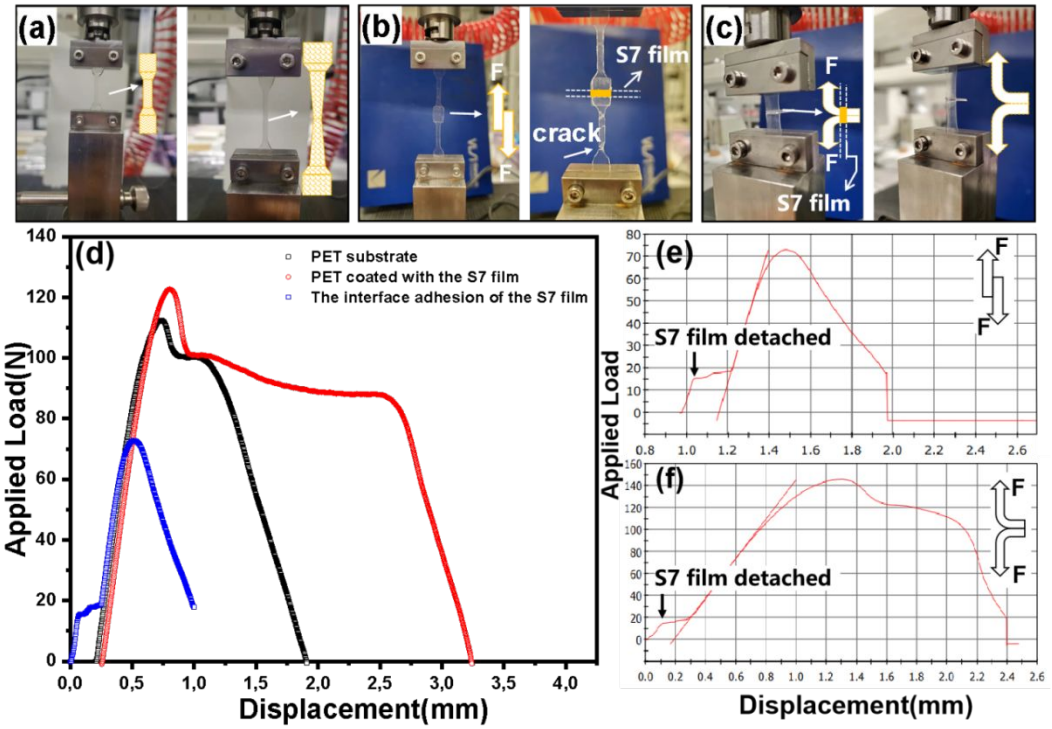

Figure 4. (a-c) The mechanical performance of each sample was investigated utilizing tensile testing. (d-f) The typical force-displacement curves of the samples were investigated.

The uniform surface morphology of the S7 grid film without penetrated cracks was observed by an SEM (Figure 5a). The 75 mol% CeO_{2-x}-TiO_2 particles within the film were naturally spherical (Figure 5 a_1&a_2). The cross-sectional SEM images of the fractured S7 grid film were displayed in Figure 5b&b_1-$_2$, which presented many laminated cracks along the thickness direction, and the XG bridging fibers and flow track of adhesive XG mixed with the 75 mol% CeO_{2-x}-TiO_2 particles around the cracks (Figure 5b_2). The thickness of the grid films was 5~10 μm evaluated by the SEM image of cross-section of the grid film in Figure 5b. The XG/HA/PAA top layer exhibited self-healing characteristics towards wounds caused by external forces as well (Figure S-3). The molecular structure of XG was similar to cellulose,

having excellent viscoelasticity and shear strain resistance[31]. Therefore, the high interfacial bonding and self-healing performance of the S7 grid film were attributed to the high viscoelasticity of XG as the gap bridged and sufficient free hydroxyl groups were derived from the PAA and HA to reform H-bonds across the interfaces. Additionally, the hexagonal mesh of the CeO_{2-x}-TiO_2/PVP framework provided an effective energy barrier for impeding cracking propagation in the S7 grid film. The water contact angles of blank glass slides, blank PET foils, flat films, and grid films were analyzed and displayed in Figure 5c. The four different components of both flat films and grid films were investigated and prepared by using the inks containing CeO_{2-x} (S2), TiO_2 (S5), 50 mol% CeO_{2-x}-TiO_2 (S3), and 75 mol% CeO_{2-x}-TiO_2 (S7) particles. The S2 and S7 flat films displayed super-hydrophilicity in natural light. The water contact angle (θ) of the S2 and S7 grid films was around 8~10°, indicating that the grid films also had hydrophilic surfaces (Figure S-4). The S5 flat films and S5 grid films differed substantially in the θ values, and the S5 grid films displayed a hydrophobic surface with θ=92°. As shown in Figures S-3(a) and Figure S-5(a), cracking of the flat films is an inevitable problem of inorganic-based coatings during drying and application, which could greatly reduce the fogging resistance and light transmittance. The hexagonal mesh effectively prevented the grid films from cracking (Figures 5a&S5b) because of the alleviated stress concentration[33].

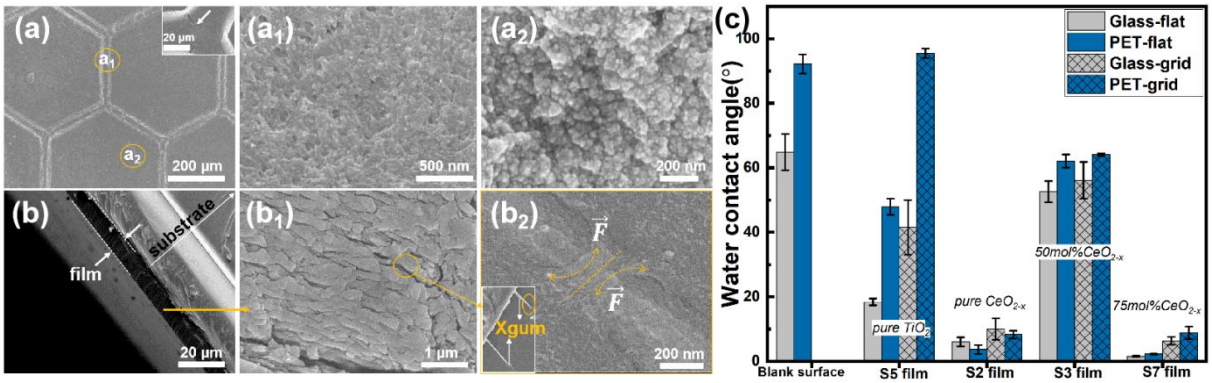

Figure 5. SEM images of (a, a_1, a_2) surface morphology and (b, b_1, b_2) cross-sectional microstructure of the grid film with the large hexagonal mesh. (c) Water contact angles of blank glass slides, blank PET foils, flat films, and grid films. The four different components of both flat and grid films were investigated and prepared using the inks made of TiO_2, CeO_{2-x}, 50 mol% CeO_{2-x} -TiO_2, and 75 mol% CeO_{2-x} -TiO_2 particles. The thickness of the grid films was 5-10 μm.

The anti-fog property of glass slides and PET foils coated with the grid films was analyzed (Figure S-6). These coated glass slides remained clear, but the fog was instantaneously observed on the blank glass slides (Figure S-6). It is noted that the words under the grid films were still clearly readable after 5 min. Then, this situation was maintained for a long time related to the

grid film's thickness. The grid films will lose their anti-fog ability when they reach the swelling equilibrium of water. In addition, a prolonged anti-fog test was performed on the PET foils coated with the S7 grid films that were stored in an incubator at 37 °C with 100 % humidity for 72 h. The grid films S7 were free of water mist and droplets, achieving good light transmittance and transparency compared with the blank PET (Figure S-6e&f). Hydrophilic surface and uniform film without cracking can ensure high light transmittance and fogging resistance. The free hydroxyl groups of PAA and HA polymers can provide a short-time hydrophilic surface rather than long-term hydrophilicity because of the low saturation of water adsorption [8,10]. Using this CeO_{2-x}-TiO_2 mixed system, TiO_2 can be modified to respond to the visible wavelength (Figure 1h). Pavasupree et al.[21] reported that the 50 mol% CeO_{2-x}-TiO_2 had a photocatalytic activity about 2-3 times higher than pure CeO_2, while nanosized TiO_2 materials had no catalytic activity under natural light. The films containing 75 mol% CeO_{2-x}-TiO_2 nanoparticles can obtain hydrophilic groups due to photocatalytic activity in natural light, therefore providing fogging resistance. The films prepared using the S7 inks with 75 mol% CeO_{2-x}-TiO_2 nanoparticles achieved the minimum water contact angle, having optimized anti-fog performance. Tap water was used for flushing the surface of the S7 flat films and S7 grid films to evaluate the interface bonding strength on the PET surface semi-quantitatively. Approximately 50 % film area remained for the S7 grid sample after 50 rinses, whereas less than 10 % of the film remained for the S7 flat sample after 3 rinses, implying the hexagonal grid film was firmly attached to the PET surface (Figure S-7).

2.4. Antibacterial efficiency

The antibacterial efficacies of S1-S7 inks containing different concentrations of TiO_2, CeO_{2-x}, and Ag^+ ions, and S8 (EtOH control solution) were analyzed against both *E. coli* and *S. aureus* by agar-diffusion test[34] (Figure 6a-d). Under visible light, S7 (containing 0.06 mol% CeO_{2-x} and 0.02 mol% TiO_2), S1 (containing XG/HA/PAA polymers as the top layer), and S2 (containing pure CeO_{2-x}) displayed strong antibacterial activity and almost completely inhibited the growth of the tested bacteria. The S5 ink (pure TiO_2) did not show antibacterial activity. The Ag-containing ink S6 reduced the colony forming unit (CFU) formation dramatically but not completely. The samples S3, S4, and S5 did not show a meaningful reduction of viable cells. The positive control S8 also failed to inhibit bacterial growth, likely due to the rapid evaporation of the ethanol loaded on the agar surface. The observed strong antibacterial activity of S1 ink can be caused by the generation of ROS, as reported previously [15,45-47].

To further analyze the antibacterial activity of S1-S8 films and quantitatively measure their antibacterial efficacy, the synthesized inks were coated on the wells of a 96-well plate, followed

by incubation with *E. coli* or *S. aureus*. Subsequently, the viable cells after the interaction were counted (Figure 7). Compared with the negative control (the uncoated wells), it was found the coatings of S3 and S7 almost completely killed the tested *E. coli* cells (more than 4 log reduction), while S1, S2, and S4 reduced the viable *E. coli* by 1.0 - 2.5 log (Figure 7a). Against *S. aureus*, only S7 coating was able to kill the bacteria completely (more than 4 log reduction), while S3 and S4 reached about 1.5 log reduction, and S1 and S2 coatings reduced the viable cells marginally (Figure 7b). Films S5 and S6 did not exhibit antibacterial activity towards either *E. coli* or *S. aureus*. Even though S6 in the form of ink showed strong bacterial growth inhibition against both *E. coli* and *S. aureus* (Figure 6b&d), the lack of antibacterial activity of S6 coatings (Figure 7a&b) indicated that Ag^+ in S6 coating could not be efficiently released to confer antibacterial property of the coating. Therefore, S7 film is the most potent against both *E. coli* and *S. aureus*. The classical agar diffusion test was performed to understand whether the excellent antibacterial activity of S7 was caused by the released active compounds or by contact killing (Figure S-8). The S7 grid film led to complete inhibition of the growth of both *E. coli* and *S. aureus*. However, no inhibition zones around the film could be observed, implying that the antibacterial mechanism could be the contact mode rather than the release mode. Most antimicrobial materials (like Ag^+ ions and ROS of TiO_2 nanoparticles) enact a release mechanism that has been well investigated. The release mode of antimicrobial activity is faster but less stable and worse durable than the contact mode[12-16]. The strong antibacterial activity of metal oxides (e.g., AgO, ZnO) mainly depended on the metal ion release content (14~100 $\mu g \cdot mL^{-1}$) and the contact area with microbes[12, 13, 16, 35]. The release contents of Ce ions in the prepared S2, S3, S4 samples are presented in Figure S-9. The S2, S3, and S7 samples showed similar Ce ions content of ~5 $\mu g \cdot mL^{-1}$ during the monitoring for 4 h of the Ce ions release for the given samples of the same amount. However, the Ce ions release of S4 was significantly lower than in other samples. Thus, Ce ions release is not the major reason for the strong antibacterial activity of the S2 and S7 inks. As such, studying the direct interactions between microbes and S1-S8 samples is necessary to unveil the antibacterial mechanism.

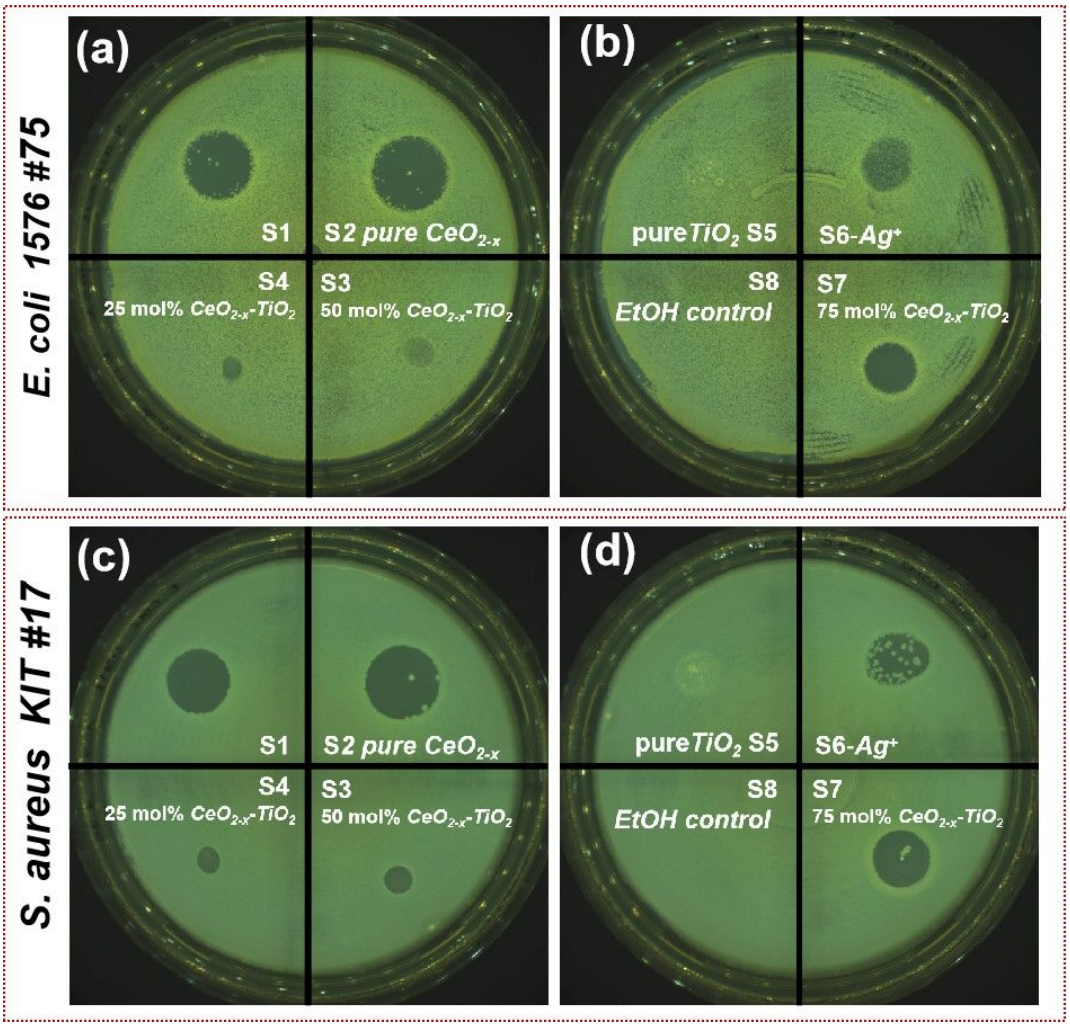

Figure 6. (a-d) Antibacterial activity of S1-S7 inks containing different concentrations of TiO_2, $CeO_{2-x,}$ and Ag^+ ions, and the EtOH control solution of S8 by growing bacteria colonies on agar plates.

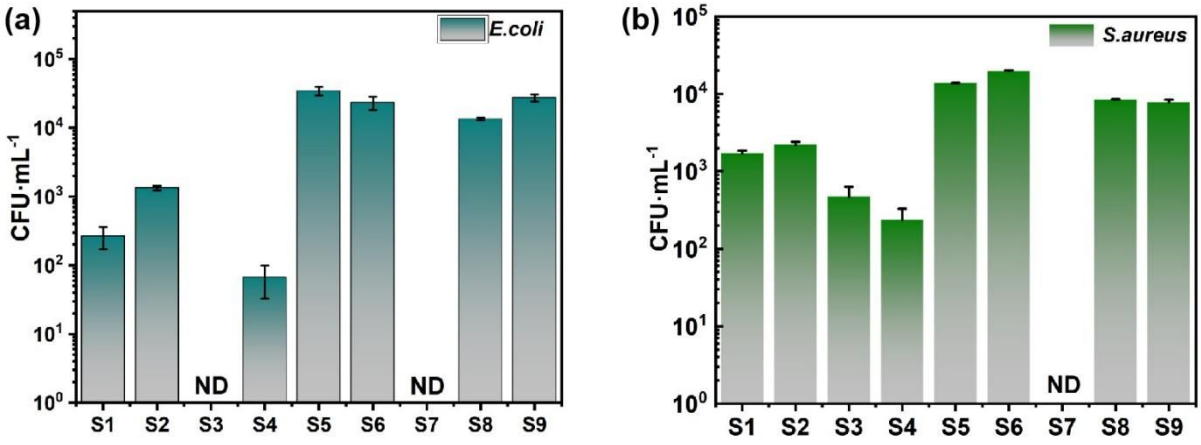

Figure 7. The viable cell number (CFU·mL^{-1}) of (a) *E. coli* and (b) *S. aureus* strains after 24 h incubation with the S1-S9.

2.5. ROS generation of the S1-S7 inks and microbial morphology on the S7 films

The bacterial intracellular ROS content in Figure 8a&b indicated that the presence of CeO_{2-x} caused significant increases in the production of ROS in *E. coli* and *S. aureus*. However, the TiO_2 would rarely motivate ROS generation in live bacteria without UV light radiation[16, 17]. The ROS content for the S2 and S7 inks that interacted with *E. coli* was one order of magnitude higher than that for the two samples that interacted with *S. aureus*. At acidic pH, Ce^{3+}/Ce^{4+} couples can exhibit high oxidase-like activity, which could promote the production of ROS. Such an effect would be enhanced by the increased Ce^{3+}/Ce^{4+} ratio[19, 20, 25]. Furthermore, due to its tunable electronic configuration of Ce^{4+} and Ce^{3+}, cerium can form mid-band gap in TiO_2, which assists the absorption in the visible region 400-500 nm (Figure S-10) [24-27]. Such also partially explains S7 containing CeO_2-x-TiO_2 possesses excellent antibacterial activity against Gram-negative and -positive bacteria (Figure 7). The ROS level produced by the S2 (CeO_{2-x}) and the S7 (CeO_{2-x}-TiO_2) further confirmed this point of view. Meanwhile, the pH values of S2 and S7 were 4.9 and 3.0, respectively (Figure S-11). The measured ROS content did not significantly differ between the empty well, S3, S4, S5 inks, and S8, respectively. These findings were consistent with the agar-diffusion test (Figure 6a-d) and bacteria viability assay (Figure 7), indicating that ROS production induced by CeO_{2-x} nanoparticles endowed the inhibitory effect of the CeO_{2-x}-TiO_2 composite inks toward bacterial growth and survival under visible light. However, it's not clear why S2 showed inconsistent results in ROS measurement and agar diffusion test. Although there was an extremely large difference in the intracellular ROS contents for *E. coli* and *S. aureus*, the antibacterial efficacy was similar. These findings suggested that the ROS mediates, but not completely, the polymer-CeO_{2-x}-TiO_2 inks induced inhibitory effects on bacterial growth and survival.

SEM morphologies were analyzed for *E. coli* and *S. aureus* from a blank glass slide and a glass slide coated with the S7 flat film (Figure 8 c&d). For *E. coli* on the S7 film, they were badly wizened and covered with granular particles (Figure $8c_2$-$_3$). *E. coli,* as an example of Gram-negative bacteria used in this work, has an outer membrane, a plasma membrane, and a periplasmic space of two or three layers of peptidoglycan, with the total cell wall being very thin (2-10 nm)[1, 2, 16, 17]. Therefore, the extremely high content of ROS (Figure 8a) could rapidly penetrate and oxidize the cell wall of Gram-negative bacteria, further leading to substantial oxidative damage to the nucleoid and cell envelope phospholipids domain[16, 17]. Some granular reaction by-products of the bio-chemical damaged cell wall, as illustrated in Figure $8c_3$. This is probably the main reason for reducing the viable *E. coli* (Figure 8a-d) after incubating overnight with the S2 and S7 inks.

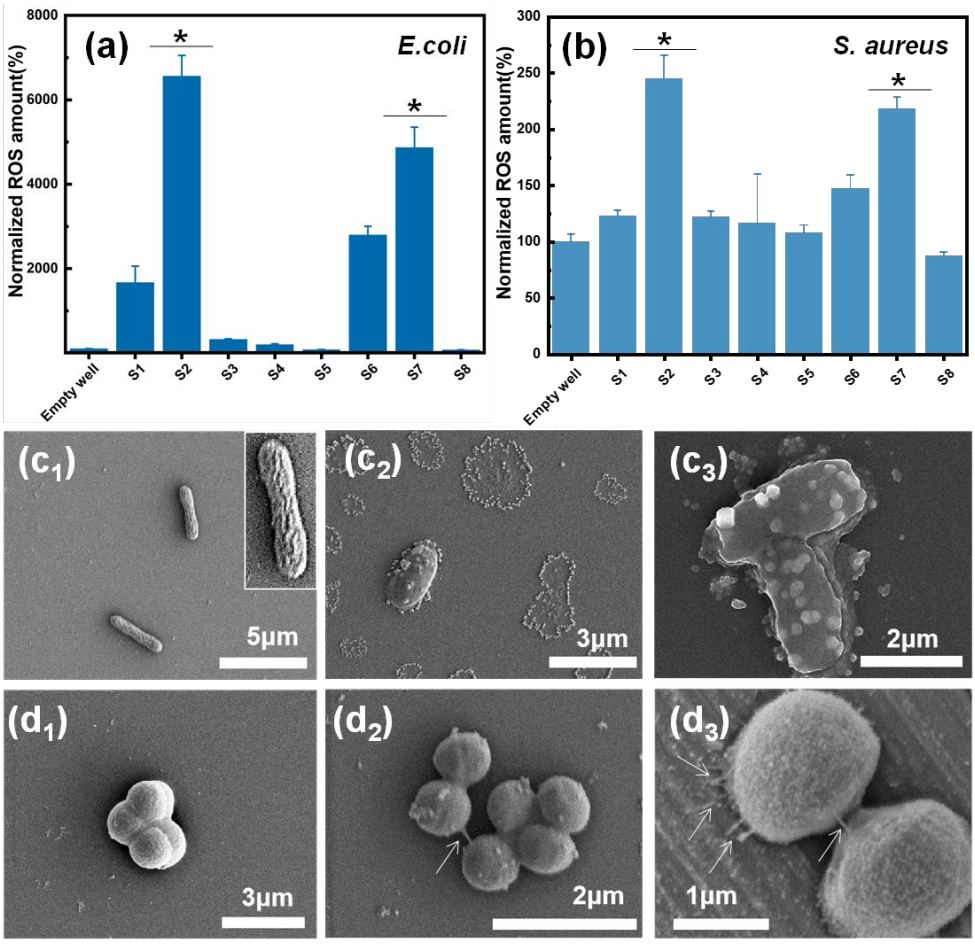

Figure 8. (a, b) Bacterial intracellular ROS content after incubation with S1-S7 inks and one control group of S8 (50 % EtOH solution). Signals obtained from the empty wells but filled with bacterial suspension were applied as the control set as 100 %. *E. coli* and *S. aureus* were incubated with the samples for 30 min. Three replicates for each sample were measured. Under the same conditions, * denotes a significant difference for ROS generated on the samples, according to Student's *t*-test ($p < 0.01$). SEM morphology of *E. coli* from (c_1) blank glass slide, (c_2, c_3) a glass slide coated with the S7 film. SEM morphology of *S. aureus* from (d_1) blank glass slide, (d_2, d_3) a glass slide coated with the S7 film.

S. aureus with slight deformation can be observed on the S7 film (Figure 8$d_{1\text{-}3}$) without critical damage compared with the *E. coli* of Figure 8c_3, suggesting the antibacterial effect of the CeO_{2-x} nanoparticles against *S. aureus* and *E. coli* were different, which was closely related to cell wall structures. The *S. aureus* strain, a Gram-positive pathogen, comprises a thick hydrophobic cell wall (20-80 nm)[13, 16, 36]. The thick cell wall of *S. aureus* is more resistant to ROS than that of Gram-negative bacteria[2, 13, 16]. Besides, similar antibacterial rate of the S7 ink for *S. aureus* and *E. coli* (Figure 6a-d), but substantially low ROS content for *S. aureus* on the S7 film (Figure 7) supported that the electrostatic attraction between Ce^{3+}/Ce^{4+} and bacteria was not the main antibacterial factor[13,14,20]. The agar diffusion assay of Figure S-8 showed no inhibition

zone around the samples, which suggested that CeO_{2-x} species leached into the growth medium during the bacterial growth were negligible to the antibacterial effects.

2.6. Adhesion force of bacteria on the S5 and S7 films

The force spectroscopy curves of the S5 and S7 films after interacting with *E. coli* and *S. aureus* for 1 min and 5 min were obtained by atomic force microscopy (AFM) in Figure 9a-d, investigating the effect of TiO_2 (S5) and 75 mol% CeO_{2-x}-TiO_2 (S7) on adhesion force and elastic properties of bacteria [6, 37, 38]. The elastic moduli estimated from the force spectroscopy curves are listed in Table1. The force spectroscopy revealed that the cell wall of both *E. coli* and *S. aureus* became less rigid, and their elastic moduli respectively decreased by about 13.7 % and 29.6 % after 5 min interaction with the S7 films. The cell-surface adhesion forces for the 5 min interaction were 1780 pN, which was more than three times higher than that for the 1 min interaction of 550 pN (Figure 9e-f). It was speculated that the effects of ROS and Ce^{3+} ions induced the changes in the chemical composition of the outer membrane and exposure of some proteins inside the envelope, which correlated with the SEM observation in Figure 9c&d[2, 13, 15, 19, 24]. No appreciable change in elastic moduli and adhesion forces were found after the bacterial interaction with the TiO_2 film even for 5min, suggesting that the cell membrane remained relative integrity, consistent with the negligible ROS content and antibacterial activity of the TiO_2 ink in visible light.

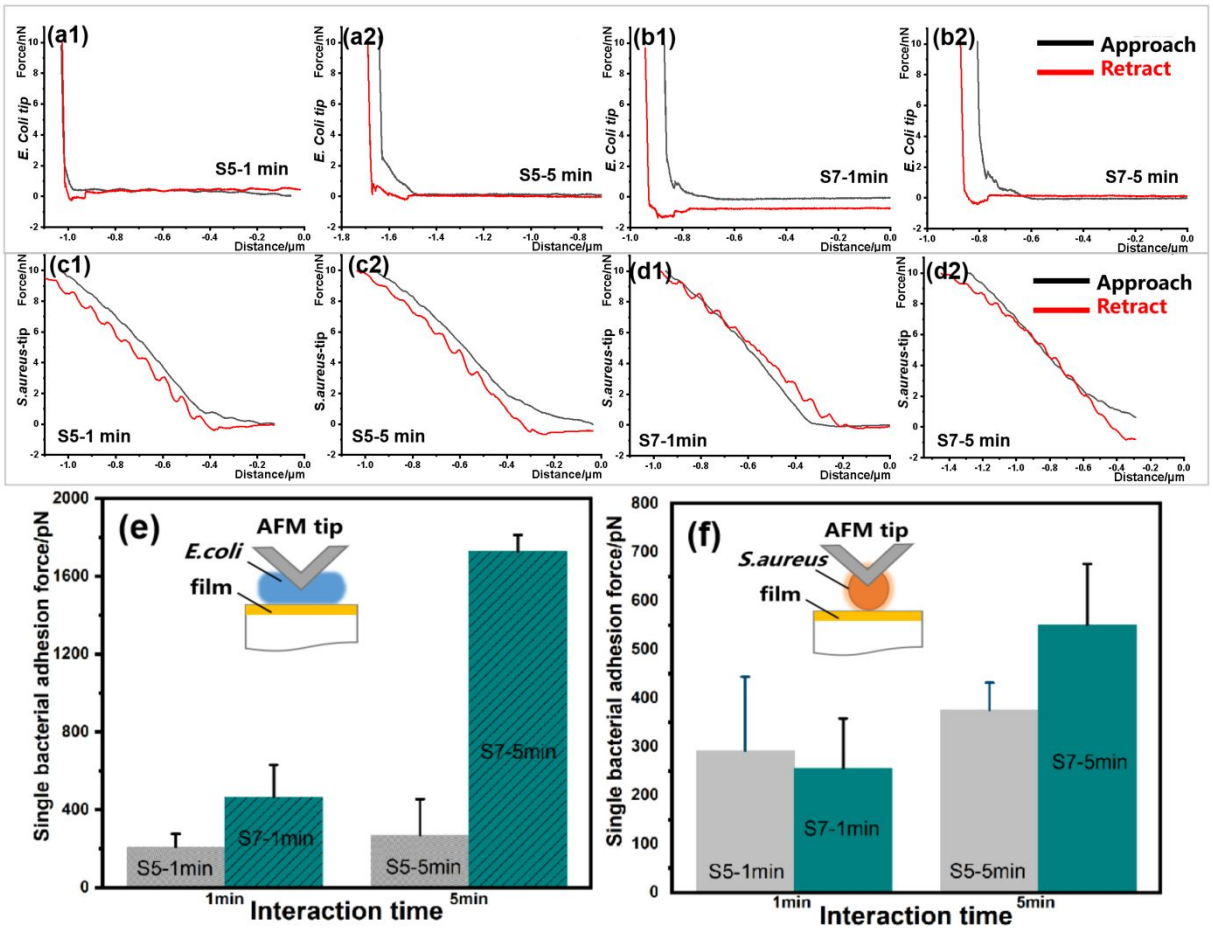

Figure 9. The force spectroscopy curves of the S5 and S7 films interacting with bacteria were examined by AFM. (a_1) S5-*E. coli*-1 min, (a_2) S5-*E. coli*-5 min, (b_1) S7-*E. coli*-1 min, (b_2) S7-*E. coli*-5 min, (c_1) S5-*S. aureus*-1 min, (c_2) S5-*S. aureus*-5 min, (d_1) S7-*S. aureus*-1 min, (d_2) S7-*S. aureus*-5 min. Based on the force spectroscopy curves, the estimated adhesion force of the S5 and S7 films interacting with (e) *E. coli* and (f) *S. aureus*.

Table 1. Elastic moduli of the S5 and the S7 films interacting with bacteria are estimated from the force spectroscopy curves shown in Figure 9(a-d).

	E. coli AFM tip				*S. aureus* AFM tip			
	S5-1min	S5-5min	S7-1min	S7-5min	S5-1min	S5-5min	S7-1min	S7-5min
Elastic Modulus (pa)	56.1	64	76.1	62.4	15.6	15	16.9	11.9
Std	3.1	3.2	3.9	5.1	0.05	0.05	0.05	0.03
R2	0.964	0.976	0.987	0.93	0.993	0.993	0.995	0.997

Recently, Liu et al.[19] verified the high triphosadenine (ATP) deprivation capacity (97%) of CeO_{2-x} nanoparticles by analyzing *in vitro* bacterial growth in medium and PBS media. The

ATP molecules were subsequently hydrolyzed to cause an intracellular starving condition, leading to cell death in apoptosis and autophagy. Therefore, the authors believed that ATP deprivation ability contributed to the *S. aureus* death after contact with the CeO_{2-x} nanoparticles due to cutting off the energy supply for bacteria. However, such an antibacterial mechanism can only work if Ce^{3+} ions penetrate the thick and waxy plasma membrane of *S. aureus*. Regretfully, there was a lack of evidence concerning ATP deprivation in bacteria. Teichoic and lipoteichoic acids (made of polyglycerol phosphate) in the cell membrane promoted adhesion and anchor wall to the plasma membrane of Gram-positive bacteria[36]. The trivalent rare-earth ions (RE^{3+}) released from rare earth oxides could strip lysosomal membrane phosphate groups and bind by the lysosomal phosphates, resulting in organelle damage[39]. The biochemical reaction led to the crystallization of $REPO_4$ on the surface of RE_2O_3 nanoparticles and morphological transformation to urchin-shaped or mesh-like structures (as shown the white arrows in Figure 8d_2-d_3) depending on the rare earth oxide species. Therefore, we propose that the Ce^{3+} ions could be firstly bound by either glycerol phosphate or ribitol phosphate groups of the cell wall of *S. aureus*, stripping the phosphate groups. The deficient cell wall and plasma membrane could provide entrances for ROS invasion. Then significant oxidation damage would occur within bacteria. XPS results indicated that the highest content of Ce^{3+} of 44.1 % occurred in the pure CeO_{2-x} particles rather than the 75 mol% CeO_{2-x}-TiO_2 nanoparticles with the Ce^{3+} of 36.8 %, but the antibacterial efficacy of >99 % occurred in the S7 inks. The antibacterial activity induced by the phosphate complexation of Ce^{3+} ions of Ce^{3+}/Ce^{4+} couples depends on Ce^{3+} concentration in the culture media, and RE_2O_3 was known to be more soluble under acidic conditions[19, 39]. The pH values of the S7 inks and the S2 inks were ~3.0 and ~4.9, respectively, which implied that the S7 inks should achieve stronger affinity with phosphate groups of the cell membranes compared with the S2 inks, resulting in the enhanced antibacterial efficiency (Figure S-10). The increased UV-Vis absorbance over the 400-800 nm wavelength shown in Figure 1 indicated that the 75 mol% CeO_{2-x}-TiO_2 nanoparticles achieved stronger photocatalytic activity than the other synthesized particles, leading to abundant hydrogen ions and hydroxyl ions decomposed from the S7 inks under natural light. Collectively, the results from XPS analysis, antibacterial rate, cell re-growth kinetics, ROS content, and SEM morphology of bacteria all indicated that the antibacterial mechanism was related to the oxidase-like activity of the CeO_{2-x}-TiO_2 and the binding capacity of cell membrane phosphate groups with ceria of high Ce^{3+} content. The inks with high Ce^{3+} content and Ti^{3+} had high oxidase-like activity, which could produce a large amount of ROS while contacting. Moreover, the Ce^{3+}/Ce^{4+} couples in acidic conditions possessed a strong reaction with either glycerol phosphate or ribitol phosphate

groups, stripping the phosphate groups of cell membranes of *S. aureus*. Based on the above mechanism, the XG stabilized grid films with 75 mol% CeO_{2-x}-TiO_2 nanoparticles exhibited excellent antibacterial activity for both *E. coli* and *S.aureus*.

2.7. Cytotoxicity

The cytotoxicity of the extracts obtained from S1-S8 inks toward normal human dermal fibroblasts (nHDFs) was displayed in Figure 10. The viable nHDFs exposed to DMEM medium containing 1 % PSN were used as a negative control and set as 100 % [16]. The cytotoxic cut-off was set as 70 % viable cells of the negative control. We observed that all the film surfaces showed more than 96 % cell viability aligned to the negative control. Thus, the treated samples did not exhibit a cytotoxic effect after 24 h.

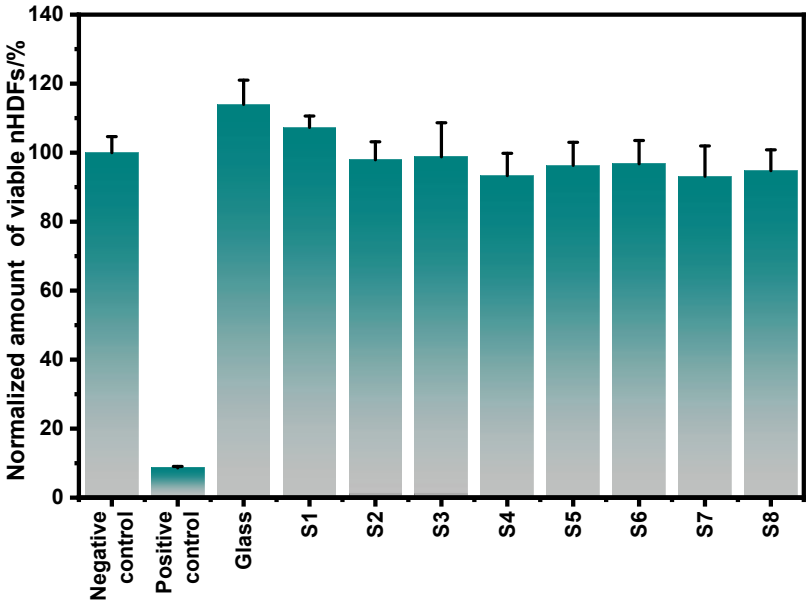

Figure 10 Cytotoxicity of extracts obtained from the S1-S8 inks toward nHDFs. Error bars display the standard deviations from 3 replicates of three technical repeats for each in one experiment.

3. Conclusions

The CeO_{2-x}-TiO_2 nanoparticles with crystalline size of 3-5 nm were synthesized using a microwave reaction in an organic bath. The UV-Vis absorption spectrum of the CeO_{2-x}-TiO_2 nanoparticles showed high absorbance over the 400-800 nm wavelength. The novel antibacterial films comprised of the hexagonal grid of 75 mol% CeO_{2-x}-TiO_2 nanoparticles and the top layer of xanthan-gum-based polymers were prepared using a micro-stamping method. The grid film with 75 mol% CeO_{2-x}-TiO_2 nanoparticles achieved an optimized antibacterial activity of nearly 100 %, high film adhesion force, and fogging resistance. The hexagonal mesh

can prevent the grid films from cracking, which, combined with the self-healing property due to sufficient hydroxyl groups, supplied a high interface bonding strength of 6.1 ± 0.15 MPa. The anti-fog property was mainly attributed to the photo-induced super-hydrophilicity of TiO_2 doped with Ce^{3+} and self-healing property due to sufficient hydroxyl groups derived from HA and PAA. The grid film's average transmittance and diffuse transmittances were 84 % and 91.5 %, respectively, over the visible light range of 380-800 nm. The excellent antibacterial rate of the 75 mol% CeO_{2-x}-TiO_2 inks for *E. coli* was related to high ROS content produced from the oxidase-like activity, while that for *S. aureus* was mainly due to the stripping damage of cell membrane phosphate groups induced by the high Ce^{3+} ions. The long-lasting films showed very high initial bacteria-killing efficiency due to the release of ROS and retained significant antibacterial activity. The top layer cannot completely seal the release of the formed ROS and the Ce^{3+} ions. Instead, it impeded a fast release of such ROS and Ce^{3+} ions. Therefore, both the top lay and the framework can function as a reservoir for a long-term release of ROS and Ce^{3+}ions, enabling a durable antibacterial function. This work has provided not only mechanistic insight into how the anti-fog coating interacts with bacterial pathogens but also manifested translation potential for application in various fields, *e.g.*, biomedical devices, food packing, and wearable devices.

4. Experimental Methods

4.1. Materials

Titanium (IV) tetrachloride (99.9 % trace metals basis), benzyl alcohol (purity 99–100.5% (GC)), 2-amino-2-(hydroxymethyl)-1,3-propanediol (Trizma ® base, purity ≥99.7%), Ce_{III} acetylacetonate hydrate (≥99.99 % trace metal basis), $AgNO_3$ (99.9999% trace metals basis) and benzyl alcohol (anhydrous, 99.8 %), chloroform (≥ 99.8%), diethyl ether (for HPLC, ≥99.9%, inhibitor-free), ethanol (absolute), methanol (analytic grade), and acetone (for HPLC ≥ 99.8%), xanthan-gum from Xanthomonas campestris, polyvinylpyrrolidone 40 (PVP), poly(acrylic acid) (PAA, M_v ~450,000), and glass slides (size: 7.5 cm × 2.5 cm × 0.1 cm) were purchased from Sigma–Aldrich (St Louis, MO, USA). HA (hyaluronic acid from cockscomb) was purchased from abcr GmbH (Karlsruhe Germany). PDMS and PET foils (thickness: 2mm) were purchased from Shanghai Pramers Chemical Tech. Co., LTD, used as substrates. All chemicals were applied as received without further purification.

4.2 Synthesis of CeO_{2-x} and CeO_{2-x}-TiO_2 Nanoparticles

CeO_{2-x} and CeO_{2-x}-TiO_2 nanoparticles (CeO_{2-x}-TiO_2) were synthesized using a microwave-assisted nonaqueous sol-gel method. In a glovebox under argon (O_2 < 1 ppm, H_2O < 1 ppm), Ce^{III} acetylacetonate (1 mmol) was added into a 10 mL pressurized glass vessel. For the CeO_{2-x}-TiO_2 solid solutions, the Ce precursor was added to the Ti precursor solution with the three contents of 25 mol%, 50 mol%, and 75 mol%. Afterward, benzyl alcohol (5 mL) was added, and the vessel was sealed with a Teflon cap and taken out of the glove box. The reaction mixture was heated employing a microwave reactor (CEM Discover) at 210 °C for 10 min with a high, stirring rate. The as-synthesized precipitate was separated from the liquid phase by centrifugation and washed three times with acetone. After drying the powder at 60 °C overnight, it was ground in a mortar and heated in air at 300 °C for 60 min in a muffle furnace. The as-synthesized CeO_{2-x}, TiO_2, and CeO_{2-x} -TiO_2 nanocrystals were analyzed by a transmission electron microscope (JEOL JEM-2100, Japan). For the Rietveld refinement analysis, the CeO_{2-x} powder was further annealed at 500 °C for 2 h and 700 °C for 30 min. The doped powders were only annealed at 700 °C for 30 min to grow the nanoparticles and obtain sharper XRD peaks (measurement described below). EDX analysis was performed on the samples annealed at 700 °C to have a good comparison with the Rietveld refinement results. All other characterization methods were carried out on the samples obtained directly after thermal treatment at 300 °C.

4.3 Preparation of CeO_{2-x} -TiO_2 dispersion

The as-synthesized CeO_{2-x} and CeO_{2-x}-TiO_2 precipitates were washed with 30 mL chloroform three times by dispersion-centrifugation cycles. Afterward, the precipitates were washed with diethyl ether in the same way. Finally, the wet precipitates were dispersed in the mixture solvent composed of deionized water and pure ethanol by a volume ratio of 1:1, resulting in a highly stable CeO_{2-x}-TiO_2 dispersion with a concentration of 10 $g \cdot L^{-1}$.

4.4 Preparation of CeO_{2-x} -TiO_2 inks and the Xanthan-gum/HA/PAA polymer ink

The stock 50 % EtOH solution were prepared by 1:1 (v/v) 96 % EtOH/dH_2O at room temperature. The 2.5 wt.% PVP polymer solution was prepared by dissolving the PVP powder in the 50 % EtOH solution at 40 °C with magnetic stirring for 1h. The stable CeO_{2-x}, or TiO_2 or CeO_{2-x}-TiO_2 dispersion, was added dropwise into the 2.5 wt.% PVP polymer solution while stirring to obtain the clear and stable CeO_{2-x}-TiO_2 inks after ultrasonic deaeration. The five inks, containing CeO_{2-x} concentration of $\psi = 0$, 0.02, 0.04, 0.06, 0.08 $mmol \cdot L^{-1}$, were investigated.

The stock solution of xanthan-gum (XG) was prepared by dissolving the XG powder and hyaluronic acid (HA) in dH_2O at 40 °C with magnetic stirring for 24h to obtain a 1 wt.% aqueous solution by the XG/HA mass ratio of 2:1. The PAA power was dissolved in the 1 wt.% XG aqueous solution at 95 °C for 1 h to obtain a 2.0 wt.% aqueous solution. According to the reference, the 0.08 $mmol \cdot L^{-1}$ $AgNO_3$ ink was prepared by dissolving the $AgNO_3$ powder in the 2.5 wt.% PVP polymer solution and was used as the control group[2, 12, 13].

4.5. Fabrication of grid films and flat films

Poly(dimethylsiloxane) (PDMS) stamps were prepared as described in the literature[33]. Figure 1 graphically illustrates the fabrication process of the transparent polymer-CeO_{2-x}-TiO_2 grid film. First, 5 × 5 cm^2 polyethylene terephthalate foils (PET, 0.05 mm thick, Toray) and a 3 × 3 cm^2 PDMS stamp (1 cm thick) were treated in Air plasma to obtain hydrophilic surfaces. To stamp the PET surface, 2 mL of CeO_{2-x}-TiO_2 ink was then dropped by pipette around the edges of the PDMS stamp. Immediately after contact, a 780-g weight was placed on top of the stamp for 30 minutes, followed by drying at room temperature for 30 min and baking at 80 °C for 10 min to remain the CeO_{2-x}-TiO_2 framework adhered to the PET foil. In the following step, the XG/HA/PAA ink (both dissolved in 50 % EtOH solution) was similarly applied on the edges of the PDMS stamp and then dried at 80 °C for 4h. After peeling off the PDMS stamp, the transparent micro-meshed films were obtained on the glass slide or PET foils as a two-layer architecture composed of a CeO_{2-x}-TiO_2 framework and a thin topcoat of XG/HA/PAA ink. The flat films composed of the CeO_{2-x}-TiO_2 ink and the XG/HA/PAA ink were prepared on PET foils/glass slides using the dip-coating method described in references[1, 7-10] as the control group.

4.6. Surface characterization and anti-fog tests

The surface wettability of bare substrates and the polymer-CeO_{2-x}-TiO_2 grid film-coated substrates was determined by a contact angle meter (Pow-ereach, Shanghai, China). Contact angle measurements were conducted directly by using the sessile drop technique. Testing liquids were deionized water. Contact angles were automatically calculated by the equipped software implementing the Laplace–Young fit. Measurements were conducted with 3 drops of each liquid.

Scanning electron microscopy (SEM) images were recorded on a Zeiss Leo-1530. Before SEM analysis, the samples were coated with 5 nm Pt. High-resolution transmission electron microscopy (HRTEM) in both TEM and scanning (STEM) modes was performed on an FEI Talos F200X operated at 200 kV. Powder X-ray diffraction (XRD) measurements were performed on a PANalytical Empyrean equipped with a PIXcel 1D detector and Cu Kα X-ray

irradiation. X-ray photoelectron spectra (XPS) were recorded by a Sigma 2 spectrometer (Thermo Scientific) using a polychromatic Al Kα X-ray source by taking C 1s = 284.8 eV as the calibration peak. The atomic concentration was calculated from the individual peak area of Ce, Ti, and O and their respective atomic sensitivity factor. The surface topography of the films was provided by a non-contact 3D-laser profilometry (ZegageTM, Zygo, USA) with a 10x objective lens. Transmittance spectra in UV–visible spectra range were recorded using a JASCO V-770 spectrophotometer equipped with an ILN-725 integrating sphere. Attenuated total reflectance Fourier transform infrared (ATR-FTIR) spectroscopy results were obtained using a Bruker Alpha FT-IR spectrometer equipped with diamond ATR optics.

The grid films deposited on the PET foils/glass slides were placed above bakers containing 50 °C water to test anti-fog properties. The PET foils coated with the S7 grid film were placed inside an incubator at 37 °C with 100 % humidity for 72 h. Samples were then removed from the incubator (into the air with a minimum of 30% relative humidity (RH)), and placed above a meshed surface at room temperature to see if fogging or obscuring of the mesh could be observed. When multiple testing cycles were required, the samples were kept at room temperature for around 10 minutes before returning to the incubator. This test was repeated up to 10 times.

4.7 Interface adhesion test and self-healing test

The interface adhesion behavior of the grid films was studied by uniaxial tensile tests using a universal testing machine (Trapezium Shimadzu AGS-X) with standard ISO 527-1:2012 at a deformation rate of 1 mm·min^{-1} [29, 30]. The tensile specimens were prepared according to standard ISO 527-3:1995, involving the bone shape (20 mm × 3mm × 1 mm) and strip-type (20 mm × 5mm × 1 mm) as shown in Figure 4c&d. Three repeated specimens were measured to determine the final tensile properties. An anti-flushing test was performed on the surface of samples under the running tap water within the 5 cm distance to test the durability in heavy humid environments, as illustrated in Figure S-7. The self-healing performance and roughness of the polymer-CeO_{2-x}-TiO_2 films were observed via the 3D-laser profilometry.

4.8 Antimicrobial activity testing

The synthesized materials' antimicrobial activity was tested with a similarly reported method[34] against the commonly occurring pathogens, namely Gram-positive *Staphylococcus aureus* A1 mecA and Gram-negative *Escherichia coli* DSM 1576. Pre-cultures of the strains were incubated overnight in 5 mL 30 % TSB containing 0.25 % glucose and were diluted to OD_{600} 0.1 with fresh medium for re-growth. The re-growth culture was further incubated for 1.5 h to

obtain exponentially growing bacterial cells and then diluted to OD_{600} 0.001. 100 µL *E. coli* and *S. aureus* suspensions were spread on the corresponding agar plate with the EasySpiral plater. A drop of 10 µL of the synthesized ink was loaded onto the PC-Agar plate, which was incubated overnight at 37°C to observe the formation of inhibition zones. Quantitative antibacterial assays were performed in 96-well plates as previously described[40]. Briefly, 10 µL of the synthesized materials were added to coat a 96-well plate in triplicates, followed by adding 100 µL bacterial suspension in the exponential growth phase (roughly in a concentration of 10^5 $CFU{\cdot}mL^{-1}$ in 30% TSB + 0.25% Glucose). The plate was incubated at room temperature for 4 h. Afterwards, the bacterial suspension was carefully removed, and wells were washed three times with 150 µL 0.9 % NaCl. 100 µL bacterial suspensions were plated in triplicates on PC agar, and viable cells were counted after overnight growth at 37°C. Viable cells were counted after plating the bacterial culture in triplicates on PC agar after overnight growth at 37°C.

4.9 Optical observation and SEM imaging

10 µL of the eight solutions S1-S8 were investigated on the standard glass slide (∅ 6 mm), then dried overnight, which were listed in Table 2. The glass slides were coated overnight by adding 10 µL of the different solutions. After coating, all EtOH was evaporated, and the agent remained on the glass slide. Thereafter, 10 µL bacterial suspension with a concentration of 10^5 $CFU{\cdot}mL^{-1}$ was added for 4 hours. The supernatant was washed away after the incubation, and the samples were fixed in Kanovsky overnight at 4 °C to increase the chance of bacteria being maintained on the sample. After removing the Kanovsky, we washed the samples with PBS and immediately microscope the samples w/o putting a glass cover on top to avoid physical stress by which we might lose some more bacteria. The live bacteria (*E. coli* and *S. aureus*) on the bare glass slides, different glass slides coated with polymer-CeO_{2-x}-TiO_2 solutions, and the control samples were observed under an optical microscope. After the optical microscope observation, we started with the dehydration in EtOH extremely carefully. The interaction of *E. coli* on the S7 film surface was observed using a scanning electron microscope (SEM, Hitachi, S-4800, USA). Bacteria were allowed to adhere to the S7 samples with different stiffness for 4 h in PBS before being washed and fixed with 4 % paraformaldehyde (Sigma, 252549, 37 % solution, The Netherlands) and 2.5 % glutaraldehyde (Sigma Aldrich, G5882, 25 % solution, USA) for 1 h at room temperature. Dehydration was performed by immersion in different ethanol concentrations (50, 70, 80, 90, and 100 %). Samples were stored under a vacuum overnight and sputtered to obtain a 10 nm gold layer (Leica, EM ACE600, Switzerland) and finally analyzed by SEM.

Table 2 The composition of the S1-S7 inks, the S8, and the S9 control groups.

Sample No.	Solutes	Solvent
S1	XG/HA/PAA polymer solutions	50 % EtOH: DI Water in a volume ratio of 1:1
S2	pure CeO_{2-x} with 0.08 mmo·L^{-1} concentration	
S3	50 mol% CeO_{2-x}-TiO_2 with 0.08 mmo·L^{-1} concentration (Ce: Ti=1:1)	
S4	25 mol% CeO_{2-x}-TiO_2 with 0.08 mmol·L^{-1} concentration (Ce: Ti=1:3)	
S5	pure TiO_2 with 0.08 mmol·L^{-1} concentration	
S6	pure $AgNO_3$ with 0.08 mmol·L^{-1} concentration	
S7	75 mol% CeO_{2-x}-TiO_2 with 0.08 mmo·L^{-1} concentration (Ce: Ti=3:1)	
S8	the 50 % EtOH control	
S9	bare glass slides as an extra control	

4.10 Atomic force microscope (AFM) analysis

Single bacterial adhesion force was measured toward the sample surfaces following the previously reported method[37, 41, 42]. A Flex Bio-AFM and a digital pressure controller (Cytosurge, Switzerland) were applied alongside an AxioObserver Z1 inverted microscope (Carl Zeiss, Germany) to guarantee precise control. Pyramidal hollow cantilevers (Nanopipette, Cytosurge, Switzerland) of a nominal spring constant of 2 N·m^{-1} and an aperture of 300 nm at the distal end were exploited to quantify the adhesion forces of bacterium towards different samples. All the cantilevers were pre-treated with air plasma for 30 s. AFM probes were then kept in a desiccator having 1 mL of Sigmacote siliconizing reagent for 12 hours and dried at 100 °C for 60 minutes. Thereafter, the spring constant of the cantilevers was measured according to the resonance frequency in PBS buffer. The microchannel in the cantilever was pre-filled with deionized water before applying pressure through the digital pressure controller.

The spring constant and sensitivity of the cantilever were calibrated every time a cell was immobilized onto the cantilever.

Single bacterial force spectroscopies were recorded at room temperature in PBS with *E. coli* and *S. aureus*, which were added to the center region of a glass dish. Cantilevers were programmed into contact with the selected bacterium (Nanopipette) till a force-setpoint (10 nN). Once contact, a negative pressure (800 mbar) was immediately exerted to immobilize a bacterium reversibly on the cantilever. The cantilever immobilized with a bacterium was immediately transferred to a new glass dish having the sample and remained in PBS buffer. The bacterium probe was programmed to approach the surface at a speed of 1 $\mu m \cdot s^{-1}$ until the force-setpoint. To guarantee a reproducible interaction between a bacterium and a surface, such force was kept for 60 s and 300 s. The bacterium-probe was subsequently retracted at a piezo velocity of 1 $\mu m \cdot s^{-1}$, and the measured forces were meanwhile recorded. At least ten measurements were conducted for every surface, and at least five different bacterial cells were utilized for every tested surface. The adhesion force was analyzed as reported[41] with SPIP software (Image Metrology A/S, Denmark).

4.11 ROS measurement

To quantify intracellular ROS that had penetrated *E. coli* and *S. aureus*, 10 mL of the bacterial inocula (preparation see above) diluted to OD_{600} 0.01 were incubated with 2', 7'-dichlorofluorescin diacetate (H2DCFDA) at a final concentration of 50 μM for 1 h, then washed with PBS three times and subsequently diluted to approximately 10^5 $CFU \cdot mL^{-1}$. 500 μL bacterial suspension was added to a plate well containing S1-S8 ink samples, using empty wells without samples but filled with the same bacterial suspension as control. After 30 and 240 min incubation, 100 μL bacterial suspension was transferred into a 96 well plate to measure fluorescence intensity with a spectrometer (excitation/emission=485 nm/535 nm, Synergy H1, BioTek, Germany).

4.12 Metal ion release measurement

The concentrations of Ce ions in the prepared samples were determined by ICP-OES, which determined the amount of CeO_{2-x} in the grid films. The 200 μL inks (S2, S3, S4, and S7) were loaded on a 20 mm (diameter) glass slide, followed by evaporation of the solvent for about 72h. The dried samples were put into 3 mL H_2O for 4 h. Afterwards, the solution was mixed with 3 mL HNO_3, and the mixture was heated in the microwave for digestion. The digested solutions were transferred to 15 mL plastic containers and used further for the metal ion release measurement.

4.13 Cytotoxicity assay

Cytotoxic effects of S1-S8 ink samples were investigated as reported[43] using normal human dermal fibroblasts (nHDFs, female, Caucasian, skin/temple, PromoCell, C-12352). Extracts of the ink samples were prepared in DMEM (Dulbecco's Modified Eagle Medium) containing 1% penicillin/streptomycin/neomycin (PSN) with an extraction ratio of surface area per medium volume of 0.3 $mL \cdot cm^{-2}$. Negative control of DMEM containing 1 % PSN without samples was applied. The extraction process was carried out in an incubator (37 °C, 100 % humidity, and 5 % CO_2) for 1 h. nHDFs were in parallel seeded at a density of 10 000 cells per well (100 µL volume) in a 96-well plate (TPP Techno Plastic Products AG, Trasadingen, Switzerland), and incubated for 24 h at 37 °C with 5 % CO_2. Thereafter, the nHDFs were incubated with 100 µL 95 % extracts (diluted with foetal calf serum (FCS)) for 24 h. The negative control was normalized to 100 %, and cells incubated with 1 % Triton X-100 in DMEM containing 5 % FCS were evaluated as the positive control. Cell viability was determined by employing an MTS [(3-(4,5-Dimethylthiazol-2-yl)-5-(3-carboxymethoxyphenyl)-2-(4-sulfophenyl)-2H-tetrazolium), a tetrazole] assay for measuring the absorbance at 490 nm to evaluate the metabolic activity of the nHDFs.

4.14 Statistics

Statistical differences were evaluated by utilizing unpaired and two-tailed Student's *t*-test. Differences among the means were accepted as significant for $p < 0.05$.

Conflicts of interest

The authors declare no competing financial interest and give consent to publish this study.

Data availability

The data supporting this study are available from the corresponding author upon a reasonable request.

Contribution statement

Fangwei Guo: giving conceptualization and major methodology, analyzing and interpreting all data, drafting the manuscript, and revising the manuscript critically for important intellectual content.

Fei Pan: acquiring data, and analyzing and interpreting data in AFM and cytotoxicity.

Flavia Zuber: acquiring data and performing antibacterial assays and SEM imaging.

Wenchen Zhang, Tian Liu, Yali Yu, and Ruiji Zhang: acquiring data.

Markus Niederberger and Xing Zhang: revising the manuscript critically for important intellectual content.

Qun Ren: Conceptual suggestion of AFM and ROS for this study, suggesting methodology and interpretation of antibacterial activity and revising the manuscript critically for important intellectual content.

Supporting Information

Supporting Information is available from ACS publications or the author.

Acknowledgment

This work was financially supported by the Science and Technology Innovation Program of Shanghai in 2020 (Grant No. STCSM-20520714300), National Natural Science Foundation of China (Grant No. U19A2099), National Major Science and Technology Projects of China (Grant No. J2019-VIII-0003-0165), and Open Project of Shanghai Key Laboratory of Spacecraft Mechanism.

Author information

Corresponding Author

Fangwei Guo - Shanghai Key Laboratory of Advanced High-temperature Materials and Precision Forming, School of Materials Science and Engineering, Shanghai Jiao Tong University, Shanghai, 200240, China; Shanghai Key Laboratory of Spacecraft Mechanism, Shanghai,201108, China; Laboratory for Multifunctional Materials, Department of Materials, ETH Zürich, Zürich 8093, Switzerland; orcid.org/0000-0002-4996-9846; Email: fwguo2014@sjtu.edu.cn

Authors

Fei Pan - Empa, Swiss Federal Laboratories for Materials Science and Technology, Laboratory for Biointerfaces, Lerchenfeldstrasse 5, 9014 St. Gallen, Switzerland; orcid.org/0000-0002-9801-5619

Wenchen Zhang - Shanghai Key Laboratory of Advanced High-temperature Materials and Precision Forming, School of Materials Science and Engineering, Shanghai Jiao Tong University, Shanghai, 200240, China;

Tian Liu − Shanghai Key Laboratory of Spacecraft Mechanism, Shanghai,201108, China;

Flavia Zuber - Empa, Swiss Federal Laboratories for Materials Science and Technology, Laboratory for Biointerfaces, Lerchenfeldstrasse 5, 9014 St. Gallen, Switzerland; orcid.org/0000-0003-1425-5920

Xing Zhang- − Shanghai Institute of Aerospace System Engineering , Shanghai, 201108, China;

Yali Yu - Shanghai Key Laboratory of Advanced High-temperature Materials and Precision Forming, School of Materials Science and Engineering, Shanghai Jiao Tong University, Shanghai, 200240, China;

Ruiji Zhang - Shanghai Key Laboratory of Advanced High-temperature Materials and Precision Forming, School of Materials Science and Engineering, Shanghai Jiao Tong University, Shanghai, 200240, China;

Markus Niederberger - Laboratory for Multifunctional Materials, Department of Materials, ETH Zürich, Zürich 8093, Switzerland; orcid.org/0000-0001-6058-1183

Qun Ren - Empa, Swiss Federal Laboratories for Materials Science and Technology, Laboratory for Biointerfaces, Lerchenfeldstrasse 5, 9014 St. Gallen, Switzerland; orcid.org/0000-0003-0627-761X

Reference

(1) Cloutier, M.; Mantovani, D.; Rosei, F. Antibacterial Coatings: Challenges, Perspectives, and Opportunities. *Trends in Biotechnology* **2015**, *33* (11), 637-652. DOI: https://doi.org/10.1016/j.tibtech.2015.09.002.

(2) Chen, C.-Y.; Yin, H.; Chen, X.; Chen, T.-H.; Liu, H.-M.; Rao, S.-S.; Tan, Y.-J.; Qian, Y.-X.; Liu, Y.-W.; Hu, X.-K.; Luo, M.-J.; Wang, Z.-X.; Liu, Z.-Z.; Cao, J.; He, Z.-H.; Wu, B.; Yue, T.; Wang, Y.-Y.; Xia, K.; Luo, Z.-W.; Wang, Y.; Situ, W.-Y.; Liu, W.-E.; Tang, S.-Y.; Xie, H. Ångstrom-scale Silver Particle-embedded Carbomer Gel Promotes Wound Healing by Inhibiting Bacterial Colonization and Inflammation. *Science Advances* **2020**, *6* (43), eaba0942. DOI: doi:10.1126/sciadv.aba0942.

(3) Guo, R.; Wen, J.; Gao, Y.; Li, T.; Hong, Y.; Wang, H.; Niu, B.; Jiang, K. Effect of the Adhesion of Ag Coatings on the Effectiveness and Durability of Antibacterial Properties. *Journal of Materials Science* **2018**, *53* (7), 4759-4767. DOI: http://dx.doi.org/10.1007/s10853-017-1939-z.

(4) Anwar, A.; Masri, A.; Rao, K.; Rajendran, K.; Khan, N. A.; Shah, M. R.; Siddiqui, R. Antimicrobial Activities of Green Synthesized Gums-stabilized Nanoparticles Loaded with Flavonoids. *Scientific Reports* **2019**, *9* (1), 3122. DOI: 10.1038/s41598-019-39528-0.

(5) Dou, X.-Q.; Zhang, D.; Feng, C.; Jiang, L. Bioinspired Hierarchical Surface Structures with Tunable Wettability for Regulating Bacteria Adhesion. *ACS nano* **2015**, *9* (11), 10664-10672.

(6) Pan, F.; Altenried, S.; Liu, M.; Hegemann, D.; Bülbül, E.; Moeller, J.; Schmahl, W. W.; Maniura-Weber, K.; Ren, Q. A Nanolayer Coating on Polydimethylsiloxane Surfaces Enables a Mechanistic Study of Bacterial Adhesion Influenced by Material Surface Physicochemistry. *Materials Horizons* **2020**, *7* (1), 93-103.

(7) England, M. W.; Sato, T.; Urata, C.; Wang, L.; Hozumi, A. Transparent Gel Composite Films with Multiple Functionalities: Long-lasting Anti-fogging, Underwater Superoleophobicity and Antibacterial Activity. *Journal of Colloid and Interface Science* **2017**, *505*, 566-576. DOI: https://doi.org/10.1016/j.jcis.2017.06.038.
(8) Jeon, Y.; Nagappan, S.; Li, X.-H.; Lee, J.-H.; Shi, L.; Yuan, S.; Lee, W.-K.; Ha, C.-S. Highly Transparent, Robust Hydrophobic, and Amphiphilic Organic–Inorganic Hybrid Coatings for Antifogging and Antibacterial Applications. *ACS Applied Materials & Interfaces* **2021**, *13* (5), 6615-6630. DOI: 10.1021/acsami.0c20401.
(9) Wang, Y.; Yao, L.; Ren, T.; He, J. Robust Yet Self-healing Antifogging/Antibacterial Dual-functional Composite Films by a Simple One-pot Strategy. *Journal of Colloid and Interface Science* **2019**, *540*, 107-114. DOI: https://doi.org/10.1016/j.jcis.2019.01.008.
(10) Han, Z.; Feng, X.; Guo, Z.; Niu, S.; Ren, L. Flourishing Bioinspired Antifogging Materials with Superwettability: Progresses and Challenges. *Advanced Materials* **2018**, *30* (13), 1704652. DOI: https://doi.org/10.1002/adma.201704652. Durán, I. R.; Laroche, G. Current Trends, Challenges, and Perspectives of Anti-fogging Technology: Surface and Material Design, Fabrication Strategies, and Beyond. *Progress in Materials Science* **2019**, *99*, 106-186. DOI: https://doi.org/10.1016/j.pmatsci.2018.09.001.
(11) Aslam, B.; Wang, W.; Arshad, M. I.; Khurshid, M.; Muzammil, S.; Rasool, M. H.; Nisar, M. A.; Alvi, R. F.; Aslam, M. A.; Qamar, M. U. Antibiotic Resistance: A Rundown of a Global Crisis. *Infection and drug resistance* **2018**, *11*, 1645.
(12) Godoy-Gallardo, M.; Eckhard, U.; Delgado, L. M.; de Roo Puente, Y. J. D.; Hoyos-Nogués, M.; Gil, F. J.; Perez, R. A. Antibacterial Approaches in Tissue Engineering Using Metal Ions and Nanoparticles: From Mechanisms to Applications. *Bioactive Materials* **2021**, *6* (12), 4470-4490. DOI: https://doi.org/10.1016/j.bioactmat.2021.04.033.
(13) Samani, S.; Hossainalipour, S. M.; Tamizifar, M.; Rezaie, H. R. In vitro Antibacterial Evaluation of Sol–gel-derived Zn-, Ag-, and (Zn + Ag)-doped Hydroxyapatite Coatings against Methicillin-resistant Staphylococcus aureus. *Journal of Biomedical Materials Research Part A* **2013**, *101A* (1), 222-230. DOI: https://doi.org/10.1002/jbm.a.34322.
(14) Li, Z.; Lee, D.; Sheng, X.; Cohen, R. E.; Rubner, M. F. Two-Level Antibacterial Coating with Both Release-Killing and Contact-Killing Capabilities. *Langmuir* **2006**, *22* (24), 9820-9823. DOI: 10.1021/la0622166.
(15) Memar, M. Y.; Ghotaslou, R.; Samiei, M.; Adibkia, K. Antimicrobial Use of Reactive Oxygen Therapy: Current Insights. *Infection and drug resistance* **2018**, *11*, 567.
(16) Pan, F.; Altenried, S.; Zuber, F.; Wagner, R. S.; Su, Y.-H.; Rottmar, M.; Maniura-Weber, K.; Ren, Q. Photo-activated Titanium Surface Confers Time Dependent Bactericidal Activity towards Gram Positive and Negative Bacteria. *Colloids and Surfaces B: Biointerfaces* **2021**, *206*, 111940.
(17) Verdier, T.; Coutand, M.; Bertron, A.; Roques, C. Antibacterial Activity of TiO2 Photocatalyst Alone or in Coatings on E. coli: The Influence of Methodological Aspects. *Coatings* **2014**, *4* (3), 670-686.
(18) Cado, G.; Aslam, R.; Séon, L.; Garnier, T.; Fabre, R.; Parat, A.; Chassepot, A.; Voegel, J.-C.; Senger, B.; Schneider, F.; Frère, Y.; Jierry, L.; Schaaf, P.; Kerdjoudj, H.; Metz-Boutigue, M.-H.; Boulmedais, F. Self-Defensive Biomaterial Coating Against Bacteria and Yeasts: Polysaccharide Multilayer Film with Embedded Antimicrobial Peptide. *Advanced Functional Materials* **2013**, *23* (38), 4801-4809. DOI: https://doi.org/10.1002/adfm.201300416. Hu, R.; Li, G.; Jiang, Y.; Zhang, Y.; Zou, J.-J.; Wang, L.; Zhang, X. Silver–Zwitterion Organic–Inorganic Nanocomposite with Antimicrobial and Antiadhesive Capabilities. *Langmuir* **2013**, *29* (11), 3773-3779. DOI: 10.1021/la304708b. Hegemann, D.; Hanselmann, B.; Zuber, F.; Pan, F.; Gaiser, S.; Rupper, P.; Maniura-Weber, K.; Ruffieux, K.; Ren, Q. Plasma-deposited AgOx-doped TiOx Coatings Enable Rapid Antibacterial Activity based on ROS Generation. *Plasma Processes and Polymers n/a* (n/a), e2100246. DOI: https://doi.org/10.1002/ppap.202100246.

(19) Zhang, H.; Qiu, J.; Yan, B.; Liu, L.; Chen, D.; Liu, X. Regulation of Ce (Ⅲ) / Ce (Ⅳ) Ratio of Cerium Oxide for Antibacterial Application. *iScience* **2021**, *24* (3), 102226. DOI: https://doi.org/10.1016/j.isci.2021.102226.
(20) Herget, K.; Hubach, P.; Pusch, S.; Deglmann, P.; Götz, H.; Gorelik, T. E.; Gural'skiy, I. A.; Pfitzner, F.; Link, T.; Schenk, S.; Panthöfer, M.; Ksenofontov, V.; Kolb, U.; Opatz, T.; André, R.; Tremel, W. Haloperoxidase Mimicry by CeO2−x Nanorods Combats Biofouling. *Advanced Materials* **2017**, *29* (4), 1603823. DOI: https://doi.org/10.1002/adma.201603823.
(21) Pavasupree, S.; Suzuki, Y.; Pivsa-Art, S.; Yoshikawa, S. Preparation and Characterization of Mesoporous TiO2–CeO2 Nanopowders Respond to Visible Wavelength. *Journal of Solid State Chemistry* **2005**, *178* (1), 128-134. DOI: https://doi.org/10.1016/j.jssc.2004.10.028.
(22) Ye, J.; Li, B.; Li, M.; Zheng, Y.; Wu, S.; Han, Y. ROS Induced Bactericidal Activity of Amorphous Zn-doped Titanium Oxide Coatings and Enhanced Osseointegration in Bacteria-infected Rat Tibias. *Acta Biomaterialia* **2020**, *107*, 313-324. DOI: https://doi.org/10.1016/j.actbio.2020.02.036.
(23) Shekunova, T. O.; Lapkina, L. A.; Shcherbakov, A. B.; Meshkov, I. N.; Ivanov, V. K.; Yu. Tsivadze, A.; Gorbunova, Y. G. Deactivation of Singlet Oxygen by Cerium Oxide Nanoparticles. *Journal of Photochemistry and Photobiology A: Chemistry* **2019**, *382*, 111925. DOI: https://doi.org/10.1016/j.jphotochem.2019.111925.
(24) Korsvik, C.; Patil, S.; Seal, S.; Self, W. T. Superoxide Dismutase Mimetic Properties Exhibited by Vacancy Engineered Ceria Nanoparticles. *Chemical Communications* **2007**, (10), 1056-1058, 10.1039/B615134E. DOI: 10.1039/B615134E.
(25) Korschelt, K.; Schwidetzky, R.; Pfitzner, F.; Strugatchi, J.; Schilling, C.; von der Au, M.; Kirchhoff, K.; Panthöfer, M.; Lieberwirth, I.; Tahir, M. N.; Hess, C.; Meermann, B.; Tremel, W. CeO2−x Nanorods with Intrinsic Urease-like Activity. *Nanoscale* **2018**, *10* (27), 13074-13082, 10.1039/C8NR03556C. DOI: 10.1039/C8NR03556C.
(26) Niederberger, M. Multiscale Nanoparticle Assembly: From Particulate Precise Manufacturing to Colloidal Processing. *Advanced Functional Materials* **2017**, *27* (47), 1703647. DOI: https://doi.org/10.1002/adfm.201703647. Matter, F.; Niederberger, M.; Putz, F. Colloidal Nanocrystals: A Toolbox for Materials Chemistry. *CHIMIA* **2021**, *75* (5), 387. DOI: 10.2533/chimia.2021.387 (acccessed 2022/04/24).
(27) Chi, M.; Sun, X.; Lozano-Blanco, G.; Tatarchuk, B. J. XPS and FTIR Investigations of the Transient Photocatalytic Decomposition of Surface Carbon Contaminants from Anatase TiO2 in UHV Starved Water/Oxygen Environments. *Applied Surface Science* **2021**, *570*, 151147. DOI: https://doi.org/10.1016/j.apsusc.2021.151147.
(28) Zaharescu, M.; Wittmar, A.; Teodorescu, V.; Andronescu, C.; Wittmar, M.; Veith, M. TiO2-CeO2 Nanometric Powders Prepared by Sol-Gel Method *Zeitschrift für anorganische und allgemeine Chemie* **2009**, *635* (12), 1915-1924. DOI: https://doi.org/10.1002/zaac.200900186. Yang, H.; Zhang, K.; Shi, R.; Tang, A. Sol–Gel Synthesis and Photocatalytic Activity of CeO2/TiO2 Nanocomposites. *Journal of the American Ceramic Society* **2007**, *90* (5), 1370-1374. DOI: https://doi.org/10.1111/j.1551-2916.2007.01540.x.
(29) Pérez, E. Mechanical Performance of in vitro Degraded Polylactic acid/hydroxyapatite Composites. *Journal of Materials Science* **2021**, *56* (36), 19915-19935. DOI: 10.1007/s10853-021-06508-7.
(30) Gao, N.; Li, J.; Zhang, W.; Ma, L.; Nwokolo, I. K.; Liu, F.; Han, E.-H. Double-layer Peelable Coating with Eminent Mechanical Properties and Anti-permeability. *Progress in Organic Coatings* **2021**, *160*, 106517. DOI: https://doi.org/10.1016/j.porgcoat.2021.106517.
(31) Rosalam, S.; England, R. Review of Xanthan Gum Production from Unmodified Starches by Xanthomonas comprestris sp. *Enzyme and Microbial Technology* **2006**, *39* (2), 197-207. DOI: https://doi.org/10.1016/j.enzmictec.2005.10.019. Gilbert, L.; Loisel, V.; Savary, G.; Grisel, M.; Picard, C. Stretching Properties of Xanthan, Carob, Modified Guar and Celluloses

in Cosmetic Emulsions. *Carbohydrate Polymers* **2013**, *93* (2), 644-650. DOI: https://doi.org/10.1016/j.carbpol.2012.12.028. de Morais Lima, M.; Carneiro, L. C.; Bianchini, D.; Dias, A. R. G.; Zavareze, E. d. R.; Prentice, C.; Moreira, A. d. S. Structural, Thermal, Physical, Mechanical, and Barrier Properties of Chitosan Films with the Addition of Xanthan Gum. *Journal of Food Science* **2017**, *82* (3), 698-705. DOI: https://doi.org/10.1111/1750-3841.13653.
(32) Chen, D.; Wu, M.; Chen, J.; Zhang, C.; Pan, T.; Zhang, B.; Tian, H.; Chen, X.; Sun, J. Robust, Flexible, and Bioadhesive Free-Standing Films for the Co-Delivery of Antibiotics and Growth Factors. *Langmuir* **2014**, *30* (46), 13898-13906. DOI: 10.1021/la503684k.
(33) Liu, T.; Yan, R.; Huang, H.; Pan, L.; Cao, X.; deMello, A.; Niederberger, M. A Micromolding Method for Transparent and Flexible Thin-Film Supercapacitors and Hybrid Supercapacitors. *Advanced Functional Materials* **2020**, *30* (46), 2004410. DOI: https://doi.org/10.1002/adfm.202004410.
(34) Pan, F.; Giovannini, G.; Zhang, S.; Altenried, S.; Zuber, F.; Chen, Q.; Boesel, L. F.; Ren, Q. pH-responsive Silica Nanoparticles for Triggered Treatment of Skin Wound Infections. *Acta Biomaterialia* **2022**, *145*, 172-184. DOI: https://doi.org/10.1016/j.actbio.2022.04.009.
(35) Lemire, J. A.; Harrison, J. J.; Turner, R. J. Antimicrobial Activity of Metals: Mechanisms, Molecular Targets and Applications. *Nature Reviews Microbiology* **2013**, *11* (6), 371-384. DOI: 10.1038/nrmicro3028.
(36) Brown, S.; Jr., J. P. S. M.; Walker, S. Wall Teichoic Acids of Gram-Positive Bacteria. *Annual Review of Microbiology* **2013**, *67* (1), 313-336. DOI: 10.1146/annurev-micro-092412-155620.
(37) Pan, F.; Liu, M.; Altenried, S.; Lei, M.; Yang, J.; Straub, H.; Schmahl, W. W.; Maniura-Weber, K.; Guillaume-Gentil, O.; Ren, Q. Uncoupling Bacterial Attachment on and Detachment from Polydimethylsiloxane Surfaces through Empirical and Simulation Studies. *Journal of Colloid and Interface Science* **2022**, *622*, 419-430. DOI: https://doi.org/10.1016/j.jcis.2022.04.084.
(38) Lau, P. C. Y.; Dutcher, J. R.; Beveridge, T. J.; Lam, J. S. Absolute Quantitation of Bacterial Biofilm Adhesion and Viscoelasticity by Microbead Force Spectroscopy. *Biophysical Journal* **2009**, *96* (7), 2935-2948. DOI: https://doi.org/10.1016/j.bpj.2008.12.3943. Kasas, S.; Stupar, P.; Dietler, G. AFM Contribution to Unveil Pro- and Eukaryotic Cell Mechanical Properties. *Seminars in Cell & Developmental Biology* **2018**, *73*, 177-187. DOI: https://doi.org/10.1016/j.semcdb.2017.08.032. Hansel, C. S.; Holme, M. N.; Gopal, S.; Stevens, M. M. Advances in High-resolution Microscopy for the Study of Intracellular Interactions with Biomaterials. *Biomaterials* **2020**, *226*, 119406. DOI: https://doi.org/10.1016/j.biomaterials.2019.119406.
(39) Li, R.; Ji, Z.; Chang, C. H.; Dunphy, D. R.; Cai, X.; Meng, H.; Zhang, H.; Sun, B.; Wang, X.; Dong, J.; Lin, S.; Wang, M.; Liao, Y.; Brinker, C. J.; Nel, A.; Xia, T. Surface Interactions with Compartmentalized Cellular Phosphates Explain Rare Earth Oxide Nanoparticle Hazard and Provide Opportunities for Safer Design. *ACS Nano* **2014**, *8* (2), 1771-1783. DOI: 10.1021/nn406166n. Tian, J.; Zeng, X.; Xie, X.; Han, S.; Liew, O.-W.; Chen, Y.-T.; Wang, L.; Liu, X. Intracellular Adenosine Triphosphate Deprivation through Lanthanide-Doped Nanoparticles. *Journal of the American Chemical Society* **2015**, *137* (20), 6550-6558. DOI: 10.1021/jacs.5b00981.
(40) Wu, S.; Zuber, F.; Brugger, J.; Maniura-Weber, K.; Ren, Q. Antibacterial Au Nanostructured Surfaces. *Nanoscale* **2016**, *8* (5), 2620-2625.
(41) Mittelviefhaus, M.; Müller, D. B.; Zambelli, T.; Vorholt, J. A. A Modular Atomic Force Microscopy Approach Reveals a Large Range of Hydrophobic Adhesion Forces among Bacterial Members of the Leaf Microbiota. *The ISME journal* **2019**, *13* (7), 1878-1882.
(42) Potthoff, E.; Ossola, D.; Zambelli, T.; Vorholt, J. A. Bacterial adhesion force quantification by fluidic force microscopy. *Nanoscale* **2015**, *7* (9), 4070-4079.

(43) Pan, F.; Amarjargal, A.; Altenried, S.; Liu, M.; Zuber, F.; Zeng, Z.; Rossi, R. M.; Maniura-Weber, K.; Ren, Q. Bioresponsive Hybrid Nanofibers Enable Controlled Drug Delivery through Glass Transition Switching at Physiological Temperature. *ACS Applied Bio Materials* **2021**, *4* (5), 4271-4279.

Table Of Contents